

This document is a guide and summary to only one of the AM Bench 2022 Challenges (CHAL-AMB2022-04-MeTT). All data for this specific challenge can be found in the NIST Public Data Repository (<https://doi.org/10.18434/mds2-2587>).

- **Subcontinuum Mesoscale Tensile Test (CHAL-AMB2022-04-MeTT):** Predict subcontinuum stress strain behavior, fracture location, and width reduction of as-built IN625 meso-scale specimens.

Modelers are invited to email simulation results to AMBench@nist.gov before the deadline of 23:59 (ET) on July 15, 2022. Be sure to include the name of the challenge (**CHAL-AMB2022-04-MeTT**) in the subject line. Tabulated results using the challenge-specific templates are required. A Q&A webinar will be held on April 28, 2022. Instructions for registering are found on the website <https://www.nist.gov/ambench>. After the webinar is completed, links to the recorded presentations and to a FAQ page will be added to the website.

All evaluations of submitted modeling results will be conducted by the AM-Bench 2022 organizing committee. Award plaques will be awarded at the discretion of the organizing committee. Because some participants may not be able to share proprietary details of the modeling approaches used, we are not requiring such details. **However, whenever possible we strongly encourage participants to include with their submissions a .pdf document describing the modeling approaches, physical parameters, and assumptions used for the submitted simulations.**

Outline for this document:

1. Overview and Basic Objectives
2. Build Process and Part Design
3. Specimen Preparation
4. Experimental Details and Measurement Descriptions
5. Benchmark Challenge Problems
6. Description and Links to Associated Data
7. References

1 Overview and Basic Objectives

AMB2022-04 is a direct extension to the measurement data provided by AMB2018-01. For AMB2018-01, data were provided for laser powder bed fusion (LPBF) builds of IN625, including powder characterization, detailed information about the build process, in situ measurements during the build, ex situ measurements of the residual stresses, part distortion following partial cutting off the build plate, location-specific microstructure characterization, and microstructure evolution during a post build heat treatment. Here, these data are extended to include mechanical property data for the as-built material. An additional build plate of parts designed for mechanical testing was fabricated using the same build machine as AMB2018-01, the same alloy (different lot number), and the same bulk material scan pattern. These parts were used for macroscopic and mesoscopic mechanical testing, with additional characterization provided by X-ray Computed Tomography (XRCT) and scanning electron microscopy (SEM). All of the mechanical test specimens were measured in the as-built state, with no residual stress anneal.

2 Build Process and Part Design

The build plate reserved from AMB2018-01 and the new build plate of specimens for mechanical testing were both built on the same EOS M270.[†] The EOS M270 is referred to using the designation CBM, for commercial build machine. To the greatest extent possible, the build parameters and conditions were kept identical between the AMB2018 and AMB2022 builds, but new powder lots were required because there was insufficient IN625 powder remaining from AM Bench 2018. The new build plate is designated AMB2022-625-CBM-B1.

Feedstock Material: The new AMB2022-04 build was conducted using IN625 powder with chemical composition provided in Table I. The powders were kept sealed in the original shipment containers until use. Virgin powder was used. Chemical composition for as-built solid material was measured after the build and is also provided in Table I.

	Powder	Solid
Chemical Composition <ul style="list-style-type: none">Values in this table are taken from vendor-supplied data sheets, which utilized ASTM E1479 (inductively-coupled plasma atomic emission spectrometers) for all elements except for using ASTM E1019 (combustion) for C/S and ASTM E1019 (fusion) for O/N.All composition measurements are in mass (weight) percent.	Ni = Balance Cr = 21.54 Fe = 0.78 Mo = 9.19 Nb = 4.13 Co = 0.18 Ti = 0.38 Al = 0.32 Si = 0.14 Mn = 0.05 P < 0.01 Ta = 0.02 C = 0.02 S < 0.005 O = 0.01 N = 0.01	Ni = Balance Cr = 20.4 Fe = 1.00 Mo = 8.60 Nb = 3.83 Co = n/a Ti = 0.31 Al = 0.27 Si = 0.11 Mn = 0.06 P < 0.001 Ta = n/a C = 0.02 S = 0.009 O = n/a N = 0.21

Table I: Chemistry characterization

Build parameters: The build parameters are listed in Table II.

CBM build conditions	
Infill laser power	195 W
Infill scan speed	800 mm/s
Hatch spacing	100 μ m
Layer thickness	20 μ m
Infill laser diameter*	100 μ m D4s
Inert gas	Nitrogen
Oxygen level	\approx 0.5 %

Table II: CBM build conditions. *Estimated

Gas flow system: The CBM uses N₂ gas with low velocity flow.

Substrates: Nickel alloy IN625 AM parts are built on a full size (252 mm x 252 mm) 1045 steel alloy build plate.

Part Layout and Specimen Naming Convention: Figure 1 shows a diagram of the AMB2022-625-CBM-B1 build plate. This plate included 8 macroscale tensile specimens (T1-T8), 3 parts designed to provide material for mesoscale tensile specimens for this challenge (TH1-3), and several additional parts for general purpose use. The part labels on Figure 1 are appended to the build plate ID to provide unique identifiers for the individual parts. For example, AMB2022-625-CBM-B1-TH1 refers to the mesoscale tensile block labeled TH1 in Figure 1.

Scan Strategy: The portions of blocks TH1-TH3 used for mesoscale tensile testing and all microstructure characterization used an X-only scan strategy with no scan rotation between layers. The supporting material for these parts, which was not characterized, was built using a default scan pattern with a 67° rotation between layers, 4 mm stripe width, and default skin post-contour (120 W, 900 mm/s). A 100 mm stripe width was used, and the parts were located such that characterized material does not contain stripe boundaries.

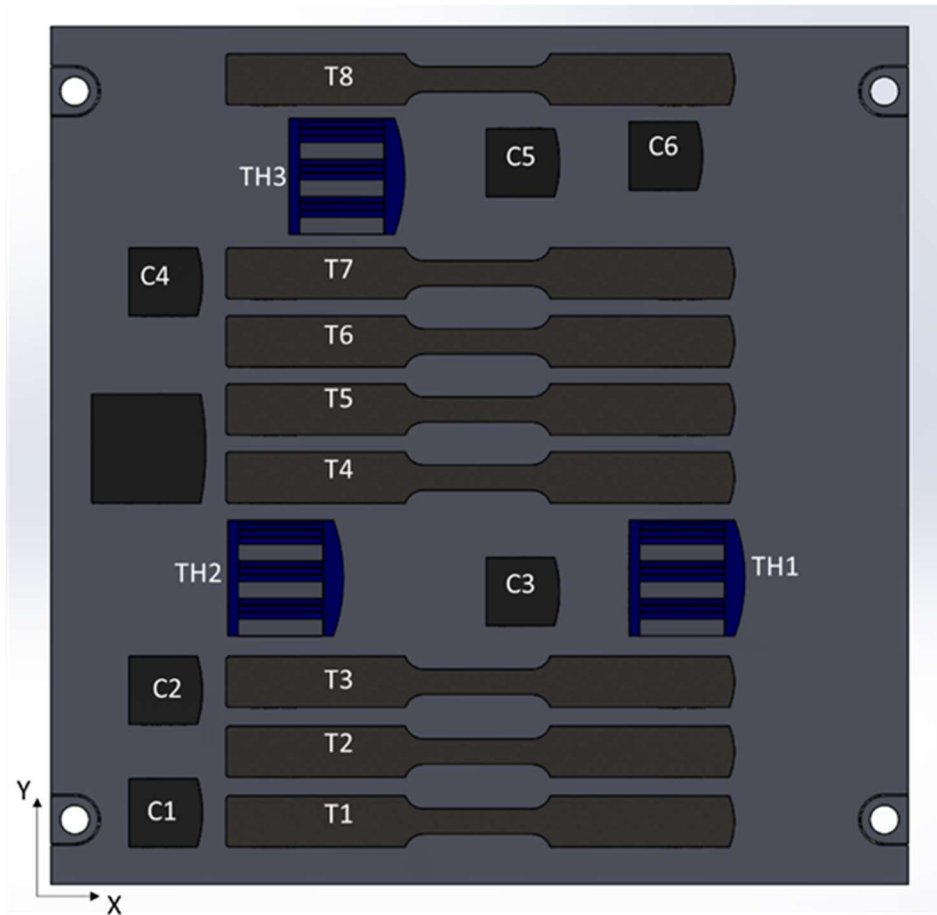


Figure 1: Diagram of AMB2022-CBM-B1 build plate

3 Specimen Preparation

No heat treatment was applied to this material. A wafer (nominal dimensions 10 mm x 24.34 mm x 0.45 mm) was cut from section F of block TH1 (Figure 2) using electric discharge machining (EDM). EDM was then used to cut a meso-tensile specimen from that wafer (Figure 2). The design of the meso-tensile specimen is from previous work [1].

The 0.45 mm thick meso-scale tensile specimen was thinned to an approximate thickness of 0.24 mm (please refer to final cross-sectional measurements with X-Ray CT) using standard polishing procedures: SiC grinding paper, 1 μ m diamond particle suspension and 50 nm colloidal silica. This sample preparation method was completed so that one side of the entire specimen and thus gauge length could be analyzed using scanning electron microscopy and is based on methods used in previous work [2]. A fiducial mark was applied to one grip section of the specimen to enable repeatable microstructural measurements before and after tensile deformation.

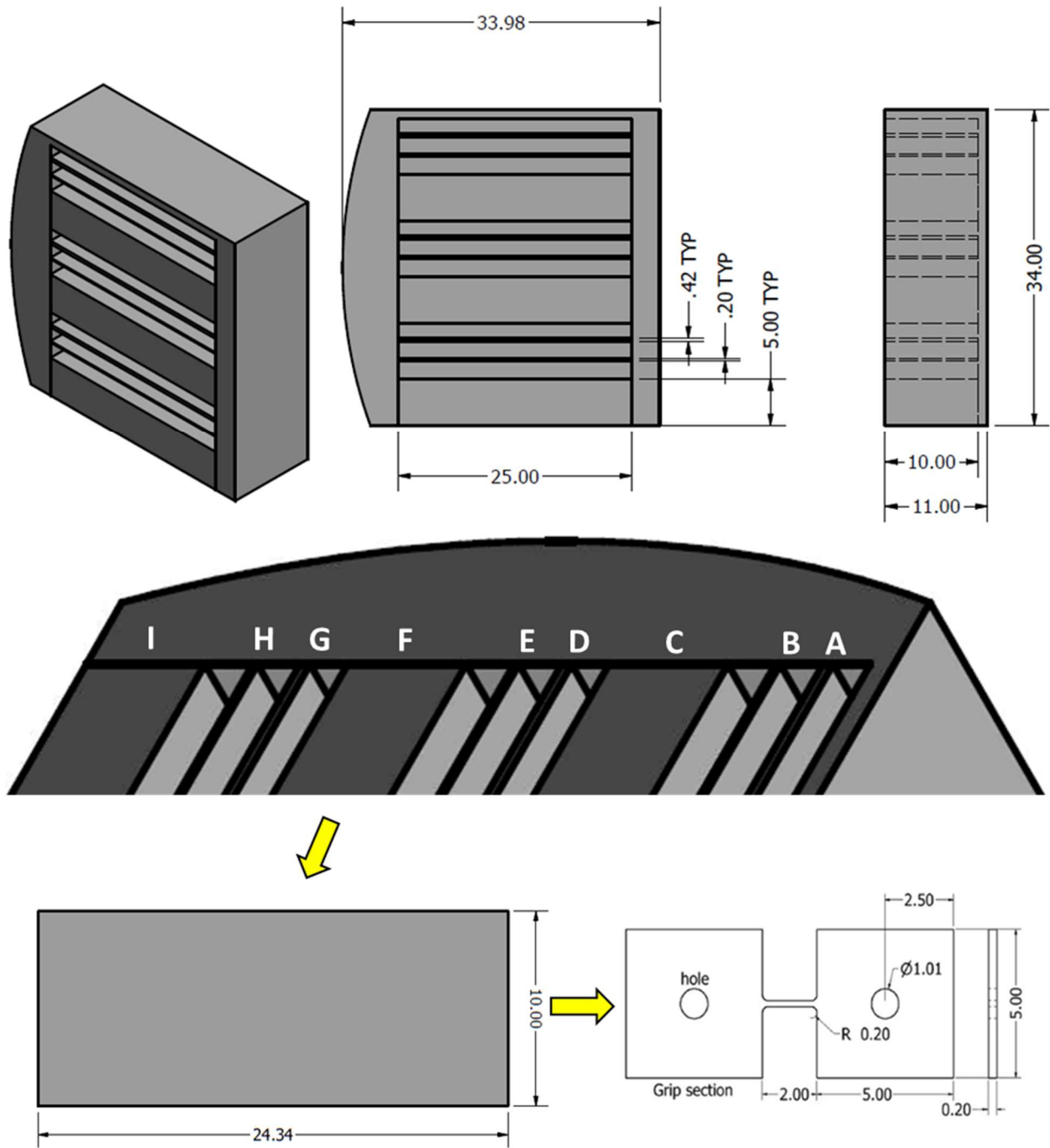


Figure 2: Schematic showing dimensions of block TH1, wafer removal from section F, and meso-tensile specimen removal from wafer. All dimensions in mm.

4 Experimental Details and Measurement Descriptions

One mesoscale tensile specimen (gauge dimensions approximately 0.2mm x 0.2 mm x 1mm) was extracted from build AMB2022-CBM-B1 specimen TH1 (Figure 1) and tested at room temperature using

a quasistatic strain rate of 0.001/s to failure. Microstructure was measured using XRCT and SEM techniques on the specimen gauge section or adjacent material. Large-area electron backscatter diffraction was used to measure crystallographic texture and grain size/morphology of the entire gauge section and two orthogonal planes. Backscatter electron imaging was used to characterize the subgrain structure and assess recast layer thickness from electric discharge machining. High energy x-ray diffraction was used to estimate dislocation density. XRCT was used to analyze the pore population as well as uncertainty in cross-sectional area for stress calculations. Literature sources were used to estimate phase fraction, residual stress, and the single crystal C-tensor.

4.1 Mesoscale Tensile Testing

The tensile tests of the mesoscale specimens are carried out using a commercial miniature universal testing stage from Fullam Inc, which was originally designed for in-situ SEM testing. (This commercial test stage was manufactured in the 1990s to early 2000's and documentation on its specifications are scarce as the vendor no longer exists.) The specimens are held in custom clevises with 1 mm-diameter pins. No through-thickness forces are applied to the specimen. Based on previous experience, deformation outside the gauge section of the meso-tensile specimen can be assumed to be negligible. The tensile tests are performed ex-situ under an optical microscope with a 2X objective lens, at a strain rate of 0.001 s^{-1} , and at room temperature. The load cell (250 N capacity, from Omega Engineering) was last calibrated in November 2019 and has a force uncertainty of 0.5 N and was rechecked in February 2022. Photographs of the test setup can be found in Ref [1]. Images are captured using a Jenoptik camera with an image resolution of 3072 x 2300 pixels. The images are analyzed offline, using digital image correlation (DIC), to obtain displacements in pixels, from which the strains are calculated. A custom DIC program is used, which has been benchmarked against a commercial DIC program (VIC2D) [3].

4.2 Electron Backscatter Diffraction

Electron backscatter diffraction (EBSD) measurements were performed on two orthogonal planes using a field emission scanning electron microscope operated with the following parameters: 20 kV accelerating voltage, 120 μm aperture, 19 mm working distance, 500 X magnification and dynamic focus. The multi-tile EBSD acquisition parameters were: 4x4 binning, 100 frames per second, multiple tiles with 5% overlap, 0.25 μm step size and the Nickel phase indexed. An example of the stitched data set from the entire gauge length (XZ plane) is provided in Figure 3. All stitched data sets are provided as .ang files for this challenge. No cleaning operations were performed on any of the EBSD data.

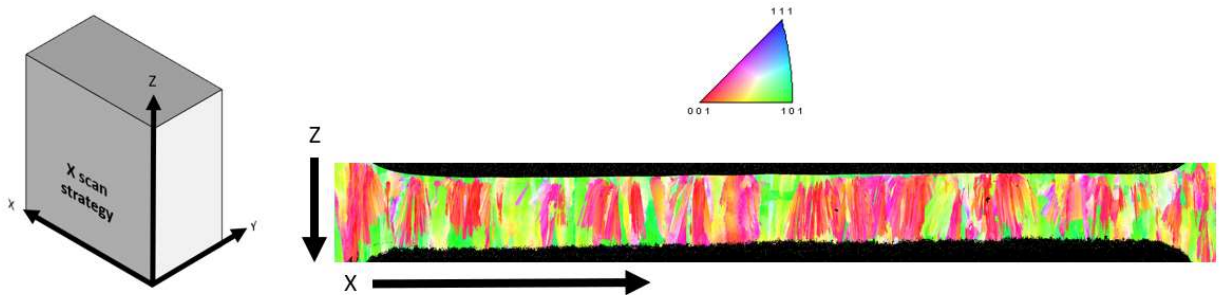


Figure 3: Inverse pole figure map of the surface microstructure across the entire gauge length of meso-scale sample TH1-F (X-only scan strategy). Tensile direction is parallel to the horizontal direction.

4.3 Backscattered Electron Imaging

Backscattered electron images were acquired with a scanning electron microscope on two orthogonal planes (XZ and XY, where Z is the build direction) using the following parameters: 20 kV accelerating voltage, 60 μm aperture, and 8.5 mm working distance. Figure 4 provides an example of the sub-grain structure, visible in the XZ plane (spacing between sub-grain structure boundaries was measured to be $0.34 \pm 0.09 \mu\text{m}$). During the EDM process, a re-cast layer is generated on surfaces that are not eventually polished, but experimental observation determined the thickness of this layer is less than 1 μm . All images of sub-grain structure and possible re-cast layer are provided for this challenge.

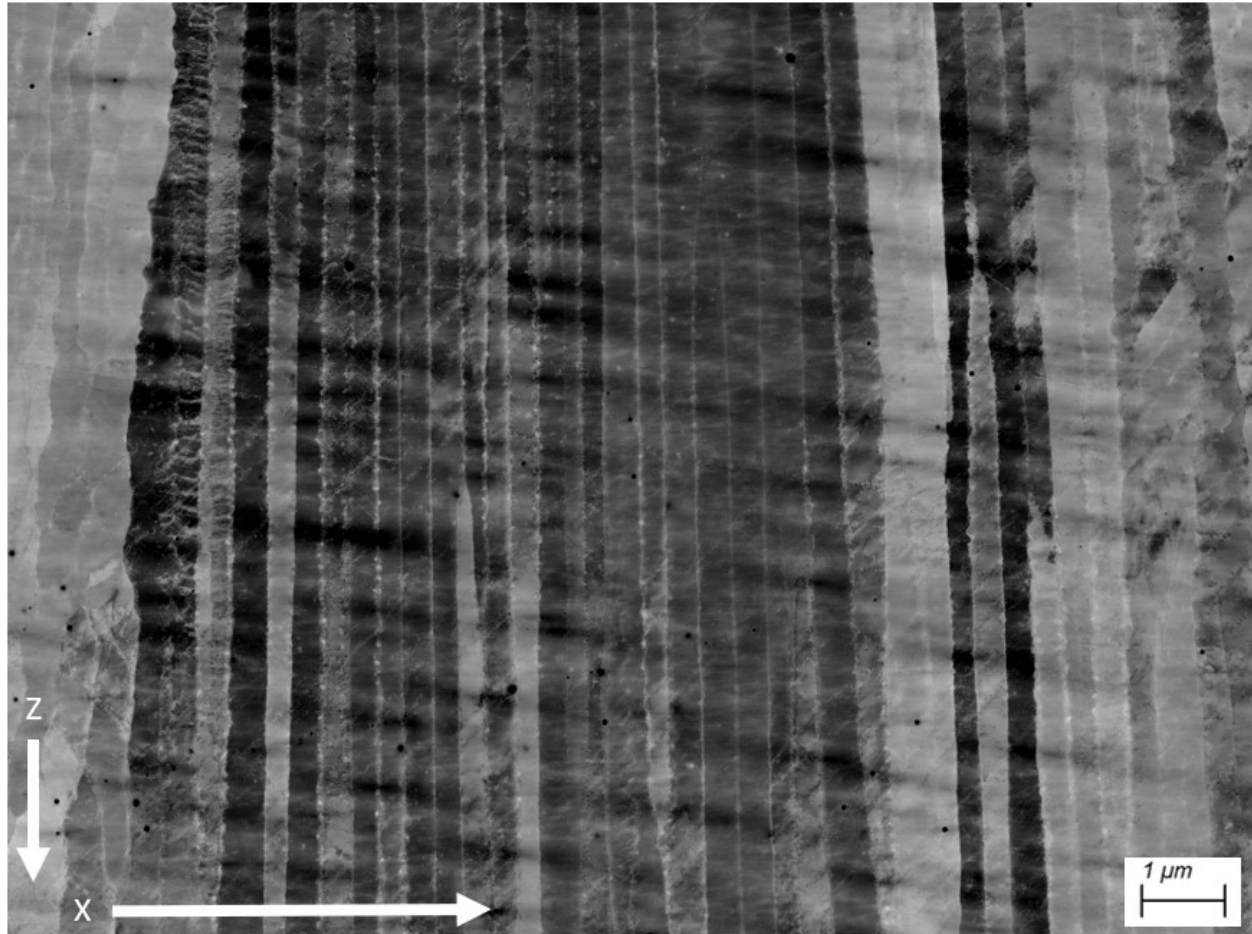


Figure 4: Representative backscattered electron image of the sub-grain structure.

4.4 High Energy X-ray Diffraction

We estimated the dislocation density in as-built Inconel 625 using high-resolution synchrotron XRD data acquired using beamline 11-BM-B at the Advanced Photon Source (APS), Argonne National Laboratory [4]. The monochromatic X-ray energy was 30 keV (wavelength $\lambda = 0.414554 \text{ \AA}$). The X-ray flux density was $\approx 5 \times 10^{11} \text{ photons s}^{-1} \text{ mm}^{-2}$. The beam size was $500 \mu\text{m} \times 200 \mu\text{m}$. We calibrated the instrument using NIST standard reference 660a (LaB_6 : lanthanum hexaboride). We thinned the samples to $\approx 100 \mu\text{m}$ in thickness and cut the thin foil into strips with an approximate dimension of $1 \text{ mm} \times 10 \text{ mm} \times 0.1 \text{ mm}$. We then loaded the strips in Kapton capillaries and mounted them on the standard sample holders of the beamline. During data collection, the samples spun rapidly in the beam (at ≈ 3000 revolutions per minute). All

measurements were conducted at room temperature (≈ 298 K). More details about the measurements can be found elsewhere [5].

For this analysis, we used XRD data acquired from sample 625-CBM-B1-P4-L4, as identified in [5] from AM Bench 2018 (same PBF-L machine and material used in AM Bench 2022, but differences in powder lot and scan strategy exist). We performed peak profile analysis of the following seven reflections of IN625 (111, 200, 220, 311, 400, 331, and 420) using pseudo-Voigt functions. We describe the centers and the full-width at half maximum (FWHM) as $2\theta_{hkl}$ and w_{hkl} , respectively, where hkl represents the Miller indices. Because the instrument has a high q resolution $\Delta q/q \approx 10^{-4}$, we neglected instrumental broadening in our analysis below. We used Scherrer's equation $D = \kappa\lambda/(w_{hkl} \times \cos(\theta_{hkl}))$ to estimate the crystallite size. Here, we chose κ at 0.94, and θ_{hkl} is one half of the diffraction angle $2\theta_{hkl}$. We then used Williamson and Smallman's method [6] to estimate the dislocation density from the peak profile of each reflection. A statistical analysis of the resulting dislocation densities yielded an estimated dislocation density of $(1.56 \pm 0.89) \times 10^{15} \text{ m}^{-2}$.

4.5 X-ray Computed Tomography

X-ray Computed Tomography (XRCT) was used to measure differences in X-ray attenuation (i.e., density) in 3D within the test specimen. The signal collected allowed for measurement of pores and changes in specimen dimensions; these two data were used to compute porosity, and cross-sectional area as a function of height (i.e., gauge length) in the specimen.

Specifically, the sub-continuum specimen was mounted "vertically" in a sample holder, such that the deformation direction is perpendicular to the resultant image slices. An XRCT scan was conducted with voxel-edge-length of approximately $1.0 \mu\text{m}$, which consisted of collecting 2401 projection images while rotating the specimen through 360° . *Vertical Stitching* mode was used to virtually increase the vertical field of view to cover the full specimen.

The resulting projection images were reconstructed and stitched together using machine-specific proprietary software (Zeiss Reconstructor Scout-and-Scan ver. 14.0.14829). Once reconstructed and stitched, the image slices were exported to a stack of grayscale, 16-bit, 2D TIFF images, where each 2D image (or *slice*) represents one voxel-height of the specimen. In total, 2022 slices were required to represent the full specimen.

The cross-sectional area and total porosity were computed after the reconstructed grayscale images were binarized. The binarization procedure is summarized below and illustrated in Figure 5:

1. Threshold the 16-bit, grayscale images. To clarify, this step is also commonly referred to as segmentation or binarization. All grayscale intensities above or equal to 33000 were made white. Note, for 16-bit grayscale images, white corresponds to a grayscale intensity of 65535. Conversely, all grayscale intensities below 33000 were made black (i.e., an intensity of 0).
2. Convert the data type to 8-bit. White pixels now correspond to a grayscale value of 255; black pixels still correspond to 0.

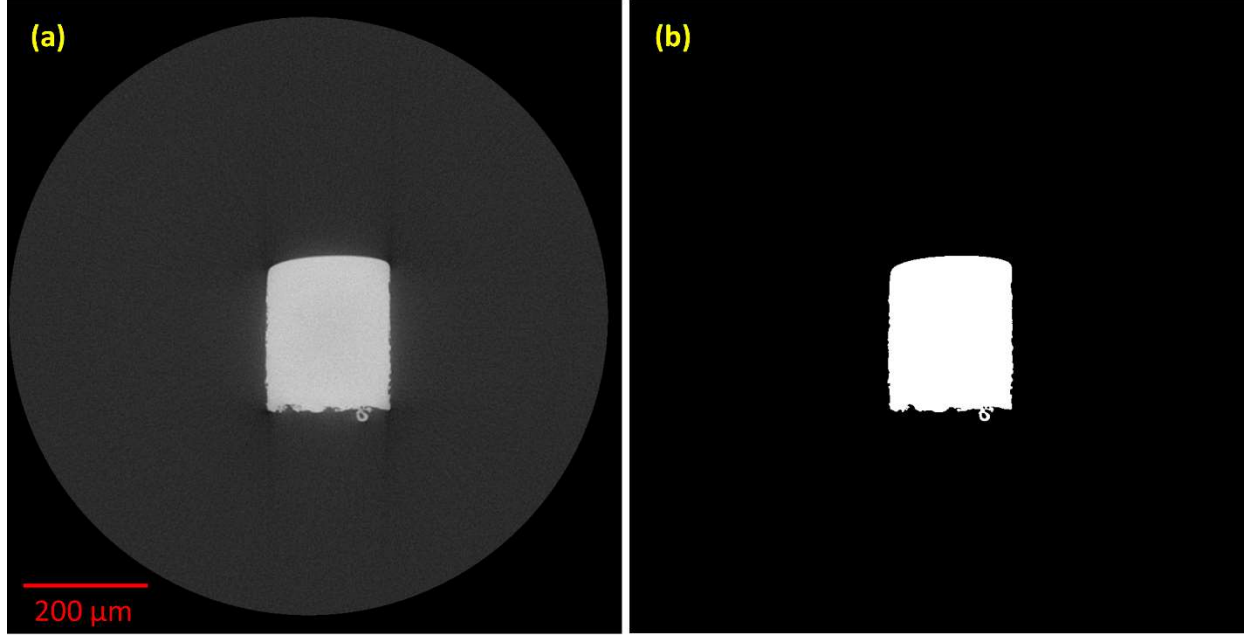


Figure 5: Post processing of one reconstructed image-slice (out of 2022), which illustrates the cross-section of the sub-continuum specimen within the gauge section. (a) An example of a reconstructed, grayscale image-slice. (b) The same image-slice after it has been segmented using a threshold intensity of 33000. The smooth top-edge corresponds to the polished surface used for backscatter electron imaging.

Additional analyses were performed to calculate the cross-sectional area and overall porosity based on these segmented images, where white pixels correspond to metal material and black pixels correspond to air/voids. Only image-slices along the gauge section, as well as a few corresponding to the initiation of the fillets, were considered for these additional analyses – more specifically, image numbers 100 through 2070 were chosen.

To calculate porosity, d_p , the following formula was used,

$$d_p = \frac{n_{void}}{n_{metal} + n_{void}}$$

where n_{metal} is the total number of white pixels (that correspond to metal material), and n_{void} is to the total number of black pixels that correspond to fully enclosed voids. Fully enclosed is taken to mean black pixels that are surrounded in 3D by white pixels based on 1-connectivity. Porosity can range from zero to one, where zero implies a perfect build absent of any (detectable) voids. For this subcontinuum sample, the porosity along the gauge length was found to be: $d_p = 0.000052032$.

The cross-sectional area as a function of relative gauge length was also calculated using the aforementioned segmented images. For each segmented image-slice, the total number of white pixels (corresponding to metal material) was summed and then converted to μm^2 using the voxel-edge-length of approximately $1.0 \mu\text{m}/\text{pixel}$. By doing this summation for each image-slice within the gauge region, the local cross-sectional area could be calculated (Figure 6). To be clear, the tensile axis of the subcontinuum sample is not guaranteed to be perfectly aligned to the cross-section illustrated in the reconstructed image-slices from XRCT due to small misalignments while mounting the sample in preparation for XRCT. As a consequence, the reconstructed image-slices are not perfectly aligned with

the cross-sectional planes of the sample. However, based on the projection images, we have estimated this misalignment error to be less than 1° .

Additional details about the XRCT parameters and the post-processing steps can be found in the “Read Me” text files found in the subdirectories of the data repository.

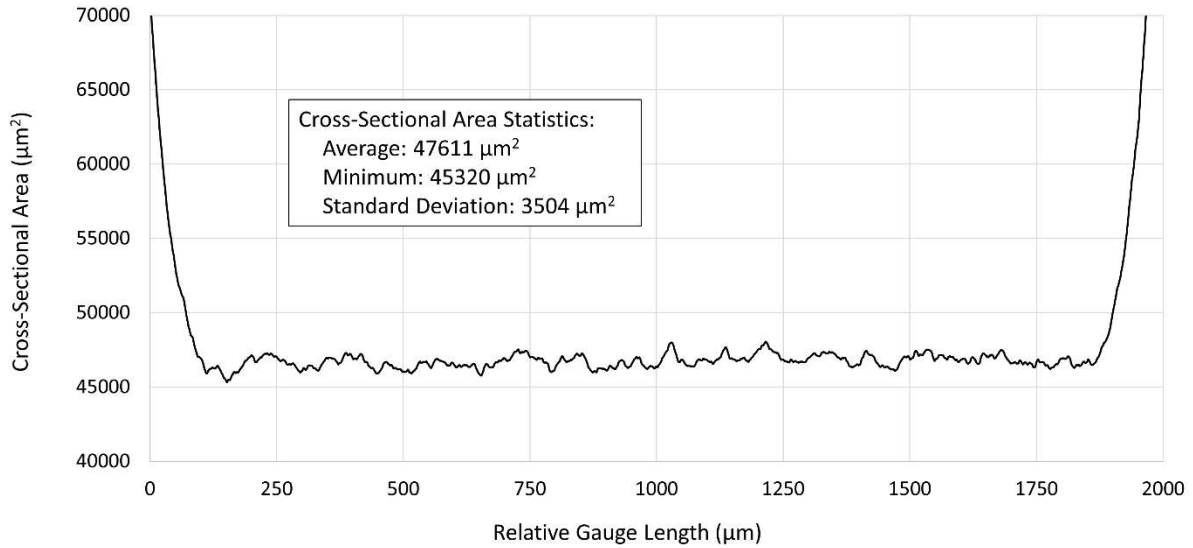


Figure 6: The cross-sectional area was calculated for each reconstructed image-slice, thereby enabling the possibility of illustrating the local cross-sectional area as a function of relative gauge length. The gauge length shown here is relative to reconstructed-image-number 100. The abrupt increase in area at both ends of the graph correspond to the transition from the (approximately) uniform gauge region to the filleted region.

4.6 Phase Fraction

We did not perform phase fraction measurements on our material, but we can assume the same phase fraction as the material from AM Bench 2018 [5], which was built on the same machine with the same material (different powder lot) and different scan strategy (XY versus X-only). The material has an FCC structure, and no secondary phases or precipitates were detected in the as-built material.

4.7 Residual Stress

We did not measure residual stress for our meso-tensile specimen, but we can assume it has the same residual stress as the material from AM Bench 2018 [7], which was built on the same machine with the same material (different powder lot) and different scan strategy (XY versus X-only). In this previous work, specifically Figure 10 [7], there is negligible macroscopic residual stress in a sample of approximate volume 2 mm x 3 mm x 3mm. As our meso-tensile specimen is much smaller than this, we feel it is appropriate to assume there is negligible macroscopic residual stress in our meso-tensile specimen.

4.8 Single Crystal C-tensor

We did not measure single crystal elastic constants for our material. We have found values in the literature that modelers may choose to use, but that is up to the modelers' discretion. The values found

in the literature are for AM Inconel 625 made via directed energy deposition (DED) and are reported as C11 = 243.3 GPa, C12 = 156.7 GPa, and C44 = 117.8 GPa [8].

5 Benchmark Challenge Problem

Modelers are invited to email simulation results to AMBench@nist.gov before the deadline of 23:59 (ET) on July 15, 2022. Be sure to include the name of the challenge (**CHAL-AMB2022-04-MeTT**) in the subject line. You must use the prediction template for this specific challenge. This excel file “prediction template CHAL-AMB2022-04-MeTT” can be found in the NIST Public Data Repository (<https://doi.org/10.18434/mds2-2587>). Grading criteria are provided on the prediction template.

Predictions are requested for the subcontinuum stress strain behavior, fracture location, and width reduction of as-built IN625 meso-scale specimen TH1-F. Separate awards will be given for the (1) stress strain behavior and (2) fracture location/width reduction predictions. For stress strain behavior, predictions of elastic modulus (E), 0.2% yield strength (YS), ultimate tensile strength (UTS), true strain at UTS, and true stress at 0.05 true strain are requested. Please use true stress and strain for all predictions. For fracture location, provide predicted distances (in micrometers) from a Reference point (left edge) of pre-deformed meso-tensile specimen EBSD map "TH1F_undeformed_left edge is origin for fracture location predictions" to the (1) left side of necking onset, (2) average fracture location, and (3) right side of necking onset. Figure 7 shows example predictions schematically. Width reduction predictions (deformed width/undeformed width, in %) are requested for post-fracture meso-tensile specimen TH1-F. Grading criteria are provided on the prediction template.

Reference point = 0 microns

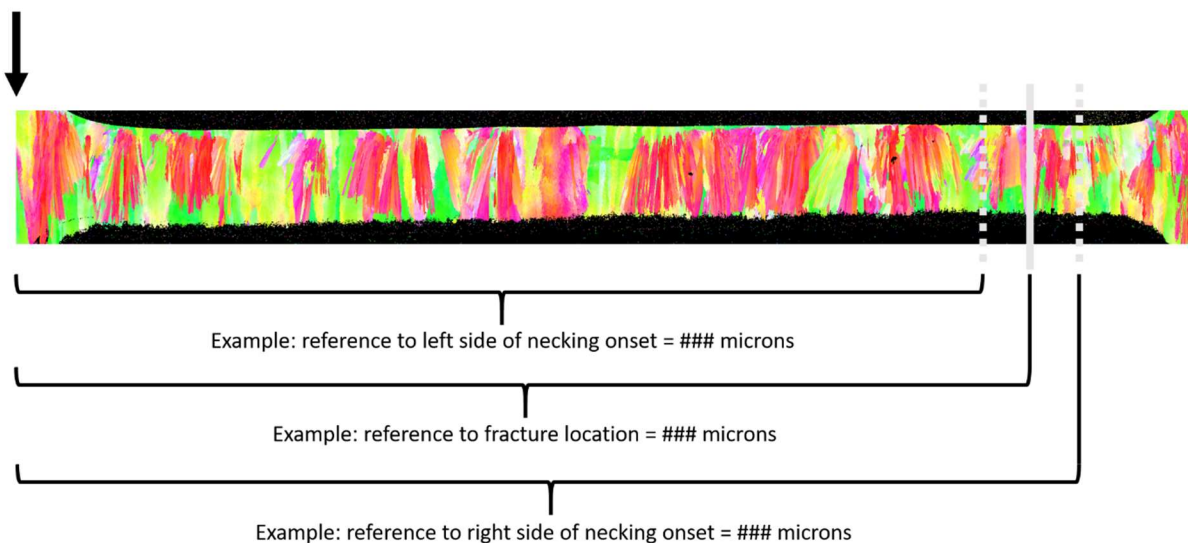


Figure 7: Schematic of necking onset and fracture location predictions

6 Description and Links to Associated Data

This document is a guide and summary to only one of the AM Bench 2022 Challenges (CHAL-AMB2022-04-MeTT). All data for this specific challenge can be found in the NIST Public Data Repository (<https://doi.org/10.18434/mds2-2587>).

7 References

- [1] Liew, L. , Read, D. , Martin, M.L. , DelRio, F. , Bradley, P. , Barbosa, N. , Christenson, T. and Geaney, J., Elastic-plastic properties of mesoscale electrodeposited LIGA nickel alloy films: microscopy and mechanics. *J. of Micromech. Microeng.* **31** (2021) 015002. <https://doi.org/10.1088/1361-6439/abc0ff>
- [2] Benzing, J.T., Liew, L.A., Hrabe, N. et al. Tracking Defects and Microstructural Heterogeneities in Meso-Scale Tensile Specimens Excised from Additively Manufactured Parts. *Exp Mech* **60**, 165–170 (2020). <https://doi.org/10.1007/s11340-019-00558-4>
- [3] Liew, L. , Read, D. , Martin, M.L. , Christenson, T. and Geaney, J., Microfabricated fiducial markers for digital image correlation-based micromechanical testing of LIGA Ni alloys. *Eng. Res. Exp.* **3** (2021) 025019. <https://doi.org/10.1088/2631-8695/abfb10>
- [4] P.L. Lee, D. Shu, M. Ramanathan, C. Preissner, J. Wang, M.A. Beno, R.B. Von Dreele, L. Ribaud, C. Kurtz, S.M. Antao, A twelve-analyzer detector system for high-resolution powder diffraction, *Journal of synchrotron radiation* **15**(5) (2008) 427-432. <https://doi.org/10.1107/S0909049508018438>
- [5] F. Zhang, L.E. Levine, A.J. Allen, S.W. Young, M.E. Williams, M.R. Stoudt, K.-W. Moon, J.C. Heigel, J. Ilavsky, Phase fraction and evolution of additively manufactured (am) 15-5 stainless steel and inconel 625 am-bench artifacts, *Integrating materials and manufacturing innovation* **8**(3) (2019) 362-377. <https://doi.org/10.1007/s40192-019-00148-1>
- [6] G. Williamson, R. Smallman, Iii. Dislocation densities in some annealed and cold-worked metals from measurements on the x-ray debye-scherrer spectrum, *Philosophical magazine* **1**(1) (1956) 34-46. <https://doi.org/10.1080/14786435608238074>
- [7] Phan, T.Q., Strantzis, M., Hill, M.R., Gnaupel-Herold, T.H., Heigel, J., D’Elia, C.R., DeWald, A.T., Clausen, B., Pagan, D.C., Ko, J.Y.P., Brown, D.W., Levine, L.E., Elastic Residual Strain and Stress Measurements and Corresponding Part Deflections of 3D Additive Manufacturing Builds of IN625 AM-Bench Artifacts Using Neutron Diffraction, Synchrotron X-Ray Diffraction, and Contour Method. *Integrating Materials and Manufacturing Innovation* (2019) 8:318–334. <https://doi.org/10.1007/s40192-019-00149-0>
- [8] Wang, Z., Stoica, A.D., Ma, D., Beese, A.M., Diffraction and single-crystal elastic constants of Inconel 625 at room and elevated temperatures determined by neutron diffraction. *Materials Science and Engineering A* (2016) 674:406-412. <https://doi.org/10.1016/j.msea.2016.08.010>

†Disclaimers

Certain commercial entities, equipment, or materials may be identified in this document to describe an experimental procedure or concept adequately. Such identification is not intended to imply recommendation or endorsement by the National Institute of Standards and Technology, nor is it intended to imply that the entities, materials, or equipment are necessarily the best available for the purpose.

The National Institute of Standards and Technology (NIST) uses its best efforts to deliver high-quality

copies of the AM Bench database and to verify that the data contained therein have been selected on the basis of sound scientific judgment. However, NIST makes no warranties to that effect, and NIST shall not be liable for any damage that may result from errors or omissions in the AM Bench databases.